Author Manuscript

Author Manuscript

Author Manuscript

Author Manuscript

HHS Public Access

Author manuscript

IEEE Trans Med Imaging. Author manuscript; available in PMC 2019 September 01.

Published in final edited form as:

IEEE Trans Med Imaging. 2018 September ; 37(9): 1989–1998. doi:10.1109/TMI.2017.2787500.

Multi-channel Acquisition for Isotropic Resolution in Magnetic Particle Imaging

Kuan Lu, **Patrick Goodwill**, **Bo Zheng**, and **Steven Conolly**

Abstract

Magnetic Particle Imaging (MPI), a molecular imaging modality that images biocompatible superparamagnetic iron oxide tracers, is well-suited for clinical angiography, in vivo cell tracking, cancer detection, and inflammation imaging. MPI is sensitive and quantitative to tracer concentration, with a positive contrast that is not attenuated or corrupted by tissue background. Like other clinical imaging techniques such as computed tomography, magnetic resonance imaging, and nuclear medicine, MPI can be modeled as a linear and shift-invariant system with a well-defined point spread function (PSF) capturing the system blur. The key difference, as we show here, is that the MPI PSF is highly dependent on scanning parameters and is anisotropic using only a single imaging trajectory. This anisotropic resolution poses a major challenge for clear and accurate clinical diagnosis. In this paper, we generalize a tensor imaging theory for multidimensional x-space MPI to explore the physical source of this anisotropy, present a multi-channel scanning algorithm to enable isotropic resolution, and experimentally demonstrate isotropic MPI resolution through the construction and use of two orthogonal excitation and detector coil pairs.

Keywords

isotropic resolution; magnetic particle imaging; multi-channel acquisition; tensor imaging theory; x-space MPI

I. Introduction

Magnetic particle imaging (MPI) is a molecular imaging modality that directly images biocompatiblesuperparamagnetic iron oxide (SPIO) tracers [1]–[4]. MPI images have positive contrast and excellent depth penetration with no background tissue signal. MPI's superb tracer sensitivity may be comparable to or even exceed that of nuclear medicine techniques [5]–[8]. However, MPI does not use ionizing radiation and the SPIO tracer is biocompatible and kidney-safe [4], [9], [10]. MPI is thus ideally suited for clinical molecular imaging applications like angiography [7], [11]–[13], cell tracking [5], [6], [14], cancer detection [15], and inflammation imaging [7].

Since the first introduction of the technique [1], there have been many significant technological advancements in instrumentation [16]–[24], particle physics [25]–[31], imaging theory and reconstruction [7], [19], [32]–[41], safety [42], [43] and developments in biomedical applications [5]–[7], [11]–[13], [44].

Author Manuscript Author Manuscript Author Manuscript Author Manuscript

Current spatial resolution in MPI, at millimeter scales, can further be improved via an array of strategies. Different efforts to improve MPI resolution and image quality have included optimizing nanoparticles for resolution and sensitivity [25], [45], simulating different trajectories for better image quality [46], proposing and building scanners with stronger gradient field [20], [32], [38], [47], [48], and signal deconvolution with a tolerable trade off in SNR loss [8].

In this work, we aim to achieve isotropic MPI resolution by analyzing the physical mechanisms behind the MPI imaging process. As we show analytically here, the MPI point spread function (PSF) is unique among imaging modalities because the image resolution is dependent on the scanning trajectory and is anisotropic with only one scanning trajectory. Fig. 1 illustrates this anisotropy. The experimental imaging "Cal" phantom (Fig. 1a) has approximately constant luminal diameter. However, when only a single excitation/receive channel is used for image acquisition (Fig. 1b and c), the resulting images show nonuniform intensity variations along the lumen. As we show in §II, these variations are highly dependent on the scanning parameters. This sort of variation make it difficult for MPI to measure blood vessel diameter in a tortuous vessel.

In order to produce robust, high-quality images, the native MPI image should not depend on scanning parameters. In this paper, we implement two orthogonal excitation and detection coils, and demonstrate theoretically and experimentally that, with proper choice of MPI scanning trajectory and image processing, we are able to make native MPI image resolution isotropic independent of the scanning trajectory, thus making it more accurate for clinical diagnosis. Our theory indicates that the linear combination of scans acquired using orthogonal MPI drive field-trajectories enables a two-dimensional isotropic image, as seen in Fig. 1d. In this paper, we first describe the theory behind MPI image anisotropy and a robust algorithm for achieving isotropic resolution, then present our multichannel hardware implementation, and finally present isotropic MPI phantom imaging results.

II. Theory

The physical mechanism and imaging theory of MPI has been well-described in literature [1], [38], and conceptual illustrations of the technique can be found in the review literature [7], [11], [49]. Briefly, a magnetic field gradient is used to magnetically saturate all SPIO particles outside a central field-free region (FFR). By translating the FFR relative to the SPIO locations, as by the use of drive coils, the SPIO magnetization can change according to Langevin physics, giving rise to a detectable signal via Faraday induction. This signal can be mapped to the instantaneous location of the FFR for image reconstruction, which is an linear and shift-invariant (LSI) technique with a well-modeled PSF [37]–[39]. We have shown this multidimensional MPI PSF to be spatially anisotropic [39].

In this section, we first investigate the source of the anisotropy inherent to the MPI PSF, then explore the necessary and sufficient conditions to produce an isotropic PSF. Finally, using a tensor formulation of the MPI x-space imaging theory, we show that the MPI PSF is highly dependent on imaging trajectory and can be made isotropic via the use of summed orthogonal scans.

Author Manuscript Author Manuscript Author Manuscript Author Manuscript

A. MPI PSF is a Combination of Two Imaging Envelopes

We have previously demonstrated theoretically and experimentally that, with baseline recovery to restore the lost DC image component along each partial field of view (pFOV) in the scan [37], MPI is a LSI system [39]. We can therefore analyze MPI resolution by exploring its PSF, which has been described in detail in [39]. Assuming that the SPIO response is instantaneous to the applied drive field, we begin with the generalized multidimensional MPI time-varying signal equation, which is dynamically dependent on the drive field:

$$\mathrm{s}(t) = \mathbf{B}_1(\mathbf{x}) \cdot m\rho(\mathbf{x}) * * * \frac{\left\|\dot{\mathbf{x}}_s(t)\right\|}{H_{sat}} \mathbf{h}(\mathbf{x}) \frac{\dot{\mathbf{x}}_s(t)}{\left\|\dot{\mathbf{x}}_s(t)\right\|} \Big|_{\mathbf{x} = \mathbf{x}_s(t)} \quad (1)$$

where x is the location vector within the imaging field of view (FOV), $\mathbf{B}_1$ (x) is the sensitivity matrix of the MPI receiver coil with form $[\mathbf{B}_{1x}(\mathrm{x})\ \mathbf{B}_{1y}(\mathrm{x})\ \mathbf{B}_{1z}(\mathrm{x})]^T$, m is the SPIO magnetic moment, ρ (x) is the SPIO particle distribution, *** is the 3D convolution operator, H_{sat} is the saturation field strength of the magnetic tracer, **h** (x) is the multidimensional MPI PSF, $\mathrm{x}_s(t)$ is the instantaneous FFR location, and $\dot{\mathrm{x}}_s(t)$ is the instantaneous FFR velocity vector, which is produced by the MPI drive coils.

For x-space image reconstruction, the MPI time signal is normalized for the FFR velocity and mapped into x-space [38], [39]. Assuming spatially homogeneous MPI receiver coils and rewriting and simplifying Eqn. 1 for spatially constant terms, the generalized MPI imaging equation becomes:

$$\hat{\rho}_{\mathbf{u}_a, \mathbf{u}_b}(\mathbf{x}) = \frac{\mathrm{s}(t) \cdot H_{sat}}{m\left\|\mathbf{B}_1\right\|\left\|\dot{\mathbf{x}}_s(t)\right\|} \quad (2)$$

$$= \mathbf{u}_b \cdot \rho(\mathbf{x}) * * * \mathbf{h}(\mathbf{x})\mathbf{u}_a(t) \Big|_{\mathbf{x} = \mathbf{x}_s(t)} \quad (3)$$

where $\hat{\rho}(\mathbf{x})$ is the reconstructed image, $\mathbf{u}_b$ is the receiver coil sensitivity unit vector, and $\mathbf{u}_a(t) = \frac{\dot{\mathbf{x}}_s(t)}{\left\|\dot{\mathbf{x}}_s(t)\right\|}$ is the scanning trajectory unit vector. Following [39], we express the PSF as:

$$\begin{aligned}\mathbf{h}(\mathbf{x}) &= \dot{\mathscr{L}}\left(\frac{\left\|\mathbf{Gx}\right\|}{H_{sat}}\right)\frac{\mathbf{Gx}}{\left\|\mathbf{Gx}\right\|}\left(\frac{\mathbf{Gx}}{\left\|\mathbf{Gx}\right\|}\right)^{\mathbf{T}}\mathbf{G} \\ &+ \frac{\mathscr{L}(\left\|\mathbf{Gx}\right\| / H_{sat})}{\left\|\mathbf{Gx}\right\| / H_{sat}}\left(\mathbf{I} - \frac{\mathbf{Gx}}{\left\|\mathbf{Gx}\right\|}\left(\frac{\mathbf{Gx}}{\left\|\mathbf{Gx}\right\|}\right)^{\mathbf{T}}\right)\mathbf{G}\end{aligned} \quad (4)$$

Author Manuscript Author Manuscript Author Manuscript Author Manuscript

where $\mathscr{L}$ is the Langevin function that describes the nonlinear particle magnetization, **G** is the gradient field matrix that has the form $\begin{bmatrix} G_x & 0 & 0 \\ 0 & G_y & 0 \\ 0 & 0 & G_z \end{bmatrix}$, and **I** is the identity matrix. Note that the terms of G are not independent, since trace[G] =0 to satisfy Maxwell's equations in a source-free region.

For analysis, we decompose this PSF into the sum of tangential and normal components:

$$\mathbf{h}(\mathbf{x}) = E_T(\mathbf{x})\mathbf{W}_T(\mathbf{x}) + E_N(\mathbf{x})\mathbf{W}_N(\mathbf{x}) \quad (5)$$

The tangential and normal components are respectively scalar envelopes E_T(x) and E_N(x) weighted by spatially varying weighting matrices $\mathbf{W}_T$(x) and $\mathbf{W}_N$(x):

$$\begin{aligned} E_T(\mathbf{x}) &= \dot{\mathscr{L}}\left(\frac{\|\mathbf{Gx}\|}{H_{sat}}\right) \\ \mathbf{W}_T(\mathbf{x}) &= \frac{\mathbf{Gx}}{\|\mathbf{Gx}\|}\left(\frac{\mathbf{Gx}}{\|\mathbf{Gx}\|}\right)^{\mathbf{T}}\mathbf{G} \qquad (6) \\ E_N(\mathbf{x}) &= \frac{\mathscr{L}(\|\mathbf{Gx}\| / H_{sat})}{\|\mathbf{Gx}\| / H_{sat}} \end{aligned}$$

$$\mathbf{W}_N(\mathbf{x}) = \left(\mathbf{I} - \frac{\mathbf{Gx}}{\|\mathbf{Gx}\|}\left(\frac{\mathbf{Gx}}{\|\mathbf{Gx}\|}\right)^{\mathbf{T}}\right)\mathbf{G} \quad (7)$$

Of the two PSF envelopes, the tangential envelope E_T(x) arises from the change in SPIO magnetic saturation and has the shape of the derivative of the Langevin curve (Eqn. 6). The normal envelope, E_N(x), arises from the rotation of the bulk magnetization to align with the time-varying magnetic field direction (Eqn. 7. E_N(x) is approximately 2.6 × worse full-width half-maximum (FWHM) spatial resolution than E_T(x). Further, E_N(x) has a slow and undesirable drop-off with distance as 1/‖**G**x‖, which manifests as a low-frequency background haze and significantly reduces image contrast and resolution.

B. A Tensor-based Theory of Multidimensional X-space MPI

A closer look at the MPI PSF shows that, while E_T(x) and E_n(x) are scalar fields, $\mathbf{W}_T$(x) and $\mathbf{W}_N$(x) are 2nd order tensors. Hence **h**(x) is also 2nd order tensor for each position x. It is important to note that **h**(x) (Eqn. 4) only depends on the tracer magnetic property H_{sat} and the gradient field strength **G**, and *is independent of scanning direction* for adiabatic particle responses [39].

Author Manuscript Author Manuscript Author Manuscript Author Manuscript

For a field-free point (FFP) scanner, the tensor PSF $\mathbf{h}(x) \in \mathbb{R}^{3\times3}$, and we can enumerate elements of the PSF tensor as scalar images $h_{ij}(x)$:

$$\mathbf{h}(\mathbf{x}) = \begin{bmatrix} h_{11}(\mathbf{x}) & h_{12}(\mathbf{x}) & h_{13}(\mathbf{x}) \\ h_{21}(\mathbf{x}) & h_{22}(\mathbf{x}) & h_{23}(\mathbf{x}) \\ h_{31}(\mathbf{x}) & h_{32}(\mathbf{x}) & h_{33}(\mathbf{x}) \end{bmatrix} \quad (8)$$

The MPI tensor image is similar in concept to diffusion tensor imaging in Magnetic Resonance Imaging (MRI), where the value at each spatial position is not a scalar intensity, but is instead a tensor comprised of directional diffusion coefficients and their covariances. We generalize the MPI imaging equation in [39] (Eqn. 12) to be the scalar nanoparticle density convolved with this tensor PSF. The resulting multidimensional MPI image $\mathbf{\Omega}(x) \in \mathbb{R}^{3\times3}$ is also a tensor, and can be expressed:

$$\mathbf{\Omega}(\mathbf{x}) = \rho(\mathbf{x}) * * * \mathbf{h}(\mathbf{x}) \quad (9)$$

$$= \begin{bmatrix} \hat{\rho}_{11}(\mathbf{x}) & \hat{\rho}_{12}(\mathbf{x}) & \hat{\rho}_{13}(\mathbf{x}) \\ \hat{\rho}_{21}(\mathbf{x}) & \hat{\rho}_{22}(\mathbf{x}) & \hat{\rho}_{23}(\mathbf{x}) \\ \hat{\rho}_{31}(\mathbf{x}) & \hat{\rho}_{32}(\mathbf{x}) & \hat{\rho}_{33}(\mathbf{x}) \end{bmatrix} \quad (10)$$

where $\rho(x)$ is the nanoparticle distribution, and $\hat{\rho}_{ij}(\mathbf{x})$ are the enumeration of each element of the multidimensional image tensor $\mathbf{\Omega}(x)$ and are individually scalar images. We note that mathematically $\hat{\rho}_{ij}(\mathbf{x}) = \rho(\mathbf{x}) * * * h_{ij}(\mathbf{x})$ and is merely the convolution of the input nanoparticle distribution with the corresponding scalar element of the PSF tensor.

C. Probing the Multidimensional Image Tensor with Drive/Receiver Field Trajectories

MPI images are formed by translating the FFR using drive field scanning trajectories and detecting the SPIO signals with a set of receiver coils with varying coil sensitivity profiles [39]. Using a drive field along an unit arbitrary trajectory vector $\mathbf{u}_a(t)$, and a receiver coil with unit coil sensitivity $\mathbf{u}_b(t)$, as in Eqn. 3, the image produced is a projection of the native tensor image $\mathbf{\Omega}(x)$ onto the two respective vectors:

$$\hat{\rho}_{\mathbf{u}_a,\mathbf{u}_b}(\mathbf{x}) = \mathbf{u}_b^{\mathbf{T}}\mathbf{\Omega}(\mathbf{x})\mathbf{u}_a(t)\,|_{\mathbf{x}=\mathbf{x}_s(t)} \quad (11)$$

where $\hat{\rho}_{\mathbf{u}_a,\mathbf{u}_b}(\mathbf{x})$ is the acquired scalar image using this set of drive and receiver trajectories.

The concept of acquiring a scalar image by projecting an imaging tensor onto predefined axes is analogous to diffusion-weighted imaging (DWI) in MRI, where the diffusion tensor

Author Manuscript Author Manuscript Author Manuscript Author Manuscript

is projected onto a predetermined axis to form a scalar image of the directional diffusivity of water only along that axis.

Current MPI instruments are built with a fixed set of excitation and reception coils along the cardinal instrument axes (e_1, e_2, and e_3). When we use one drive coil in direction e_j and one receiver coil in direction e_i, the resulting MPI image selects the scalar element $\hat{\rho}_{ij}(\mathbf{x})$ from the multidimensional tensor image $\mathbf{\Omega}$ (x). For example, if we only use drive and receiver coils along the x-direction (e_1), we get the collinear image along the instrument x-axis, which is also the 1st diagonal element $\hat{\rho}_{11}(\mathbf{x})$ of $\mathbf{\Omega}$ (x). On the other hand, if we use a y transmit coil to excite along e_2 and an x receive coil to receive along e_1, we get the transverse image $\hat{\rho}_{12}(\mathbf{x})$, which is an off-axial element of $\mathbf{\Omega}$ (x). We show $\hat{\rho}_{11}(\mathbf{x})$ and $\hat{\rho}_{12}(\mathbf{x})$ for point sources in Fig. 2, which also decomposes the PSFs into the two tangential and normal envelopes and their corresponding weighting matrices. The envelopes are radially symmetric and their FWHM determines the resolution of the PSF; whereas the weighting matrices are radially varying and asymmetric, and thus govern the anisotropy of the PSF. Notably, whereas the collinear PSF contains only positive values, the transverse PSF contains both positive and negative values, which arises from the positive and negative components in the projection of the weighting matrices on e_1 and e_2.

In practice, the excitation and detection vectors can be time-varying and along any arbitrary direction. Examples of time-varying excitation trajectories include Lissajous or spiral FFP trajectories [46]. Notably, the detection vector can also be time-varying, which is feasible through a dynamic linear combination of time-varying signals from multiple receiver coils. Eqn. 11 shows that, as a result of a time-varying excitation and receiver trajectory, the instantaneous image intensity obtained, $\hat{\rho}_{\mathbf{u}_a,\mathbf{u}_b}(\mathbf{x})$, is a linear combination of the scalar components of the tensor image $\mathbf{\Omega}$ (x) with respect to the instantaneous $\mathbf{u}_a(t)$ and $\mathbf{u}_b$.

We note that each scalar image element $\hat{\rho}_{ij}(\mathbf{x})$ has different imaging properties (see Fig. 2). Therefore, properties of the acquired image is dependent on how these scalar images are combined through differing trajectories $\mathbf{u}_a(t)$ and $\mathbf{u}_b(t)$. It becomes clear that the MPI imaging trajectory can be chosen to optimize parameters such as resolution, SNR, magnetostimulation, and scan time. In this paper, we demonstrate a choice of trajectory to improve resolution, where we use two simple linear scans to sample the elements $\hat{\rho}_{22}(\mathbf{x})$ and $\hat{\rho}_{33}(\mathbf{x})$ with no noise gain. However, this tensor imaging formulation can be easily adapted to analyze other trajectories with no mathematical difference.

D. Excitation / Reception Trajectory Dependent Anisotropy

Each scalar component of the image tensor $\hat{\rho}_{ij}$ has different directional anisotropy. This is visually apparent in Fig. 1b and c, which shows distinct differences between $\hat{\rho}_{22}$ and $\hat{\rho}_{33}$, imaged along the y and z directions in a 7 T m^{-1} FFP scanner. The reason for this is that the projection of the PSF, $\mathbf{h}(\tilde{x})$, onto the cardinal instrument axes $\vec{\mathbf{e}}_i$, namely, h_{ii} (x), is itself

Author Manuscript Author Manuscript Author Manuscript Author Manuscript

directionally anisotropic (visualized in Fig. 4a and b). Assuming a spatially homogenous detector coil sensitivity, we can decompose h_{ii}(x) using Eqns. 5 and 11:

$$h_{ii}(\mathbf{x}) = E_T(\mathbf{x})\mathbf{e}_i^{\mathbf{T}}\mathbf{W}_T(\mathbf{x})\mathbf{e}_i + E_N(\mathbf{x})\mathbf{e}_i^{\mathbf{T}}\mathbf{W}_N(\mathbf{x})\mathbf{e}_i \quad (12)$$

The envelopes E_T(x) and E_N(x) are radially isotropic regardless of the scanning trajectories (Fig. 2). The directional anisotropy of h_{ii}(x) is thus due to the projection of the weighting matrices $\mathbf{W}_T$(x) and $\mathbf{W}_N$(x) onto the excitation and detection vectors, i.e. $\vec{\mathbf{e}}_i^{\mathbf{T}}\mathbf{W}_T(\mathbf{x})\vec{\mathbf{e}}_i$ and $\vec{\mathbf{e}}_i^{\mathbf{T}}\mathbf{W}_N(\mathbf{x})\vec{\mathbf{e}}_i$ (shown in Fig. 2c and e).

E. Achieving Isotropic Resolution with Multiple Orthogonal Scans

In this section, we show that a simple summation is sufficient to eliminate MPI image anisotropy for improved resolution. The technique presented here is deterministic (e.g. does not require choice of any regularization parameters), and also reduces image noise through averaging.

We first normalize the orthogonal collinear images (i.e. $\hat{\rho}_{ii}$) by the gradient strength along each direction, then sum the resulting images together. With some effort (see Appendix A), we can prove that such a summation results in isotropic resolution. These normalization and summation operations can be succinctly expressed for a FFP imager:

$$\begin{aligned}\hat{\rho}(\mathbf{x}) &= \mathrm{trace}[\mathbf{\Omega}(\mathbf{x})\mathbf{G}^{-1}] \\ &= \sum_{i=1}^{3} \frac{\hat{\rho}_{ii}(\mathbf{x})}{G_{ii}} \\ &= \rho(\mathbf{x}) * * * (E_T(\mathbf{x}) + 2E_N(\mathbf{x}))\end{aligned} \quad (13)$$

where $\hat{\rho}(\mathbf{x})$ is the summed image and G_{ii} is the $(i, i)^{th}$ element of the gradient matrix $\mathbf{G}$.

We note in Eq. 13 that $\hat{\rho}(\mathbf{x})$ no longer has weighting matrix dependencies. Removing the $\mathbf{W}_T$(x) and $\mathbf{W}_N$(x) dependence is powerful and produces an image that *does not depend on scanning direction*. We can see the improvement in image quality as we change from anisotropic to isotropic in Figure 4, where we show the yz cross-section of two orthogonal collinear PSFs probed along y and z axes (h_{22} and h_{33}), as well as the sum of these PSFs. We also see that this holds experimentally for Figs. 1d and 6d.

F. Projection MPI Improves Resolution over 3D

For a field-free line (FFL) scanner, we only need to make some minor modifications to Eq. 9 to make it a double convolution in addition to changing the dimensionality of the matrices to $\mathbf{h}, \mathbf{\Omega} \in \mathbb{R}^{2\times 2}$.

Author Manuscript Author Manuscript Author Manuscript Author Manuscript

It is possible to extend Eq. 13 to FFL projection imaging with modest changes to the analysis [19], [20]. Again, summing the collinear images ($\hat{\rho}_{ii}$) following the method shown in the Appendix gives us an isotropic image

$$\hat{\rho}(\mathbf{x}) = \sum_{i=1}^{2} \frac{\hat{\rho}_{ii}(\mathbf{x})}{G_{ii}} = \rho(\mathbf{x}) * * (E_T(\mathbf{x}) + E_N(\mathbf{x})) \quad (14)$$

This result shows that, fundamentally, a combined image $\hat{\rho}(\mathbf{x})$ from a FFL gradient will have better resolution than a 3D FFP imager with the same gradient strength. This is because the summed image in a FFL scanner is comprised of one part E_T, which has higher spatial resolution, and one part E_N, which is lower resolution, in comparison to a FFP scanner which is the sum of one part E_T and two parts E_N.

III. Methods and Materials

A. MPI Multichannel Hardware Design

Here we describe the design and construction of multichannel drive and detector coils used to achieve isotropic resolution in X-space MPI. Here we have chosen to implement two full channels along the y and z cardinal instrument axes of a FFP 7 T/ m MPI scanner at UC Berkeley (e_2 and e_3) to partially demonstrate this concept, due to bore size and power limitations in the existing system. We chose these axes to take advantage of the natural resolution benefit along the x-axis, as the gradient strength along x is 7 T/ m, which is twice higher than that of y and z and thus yields 2-fold higher spatial resolution. Here we aligned the drive and receiver coils with the instrument axes, which enabled conventional solenoidal and saddle coil designs. Moreover, as shown in the previous section, this two-channel implementation is necessary and sufficient for isotropic resolution for FFL-based projection and 3D imaging.

We operated drive coils independently to produce linear scanning trajectories, which was capable of fully sampling the (2, 2) and (3, 3) diagonal elements of $\mathbf{\Omega}(\vec{\mathbf{x}})$, as presented in Eq. 10, separately and with no noise gain. This implementation could be further modified to form different time-varying trajectories via the use of an additional decoupling matrix in the hardware between y and z channels, to minimize channel cross-talk through the mutual inductance of the drive coils which may induce non-negligible current in the orthogonal coil and cause the drive field trajectory to differ from the desired FFR trajectory.

B. MPI Multichannel Hardware Implementation

All the experiments were performed on a FFP scanner [50] developed at UC Berkeley (Fig. 5a). To enable multichannel acquisition, we built two orthogonal excitation and receive channels. Fig. 5b) shows the two excitation coils. The transverse coil was a double layered Golay coil pair (7 turns/layer, 12.7 cm long) made out of thin copper sheet (2 mm thick) cut out by a Dremel tool (Robert Bosch Tool Corp., Germany) mounted on a robot stage programmed in MATLAB (Mathworks, MA, USA). The two layers were separated and insulated by Kapton tape (Dupont, DE, USA, 1 mil), jointed by soldering, and formed on

Author Manuscript Author Manuscript Author Manuscript Author Manuscript

G-10 tubing (ID = 2.75 in, OD = 3.15 in). On top of the transverse coil, we wound a solenoidal coil with hollow magnet wire. The transmit coil assembly was then encapsulated by heat conductive epoxy under vacuum and integrated into the scanner. Two AE 7796 power amplifiers (AE Techron Inc., IN, USA) and custom low-pass filters for feedthrough interference were connected in series to power the transmit coils. We also custom built two orthogonal receive coils with homogeneous reception in the imaging volume. Gradiometer configuration is implemented to cancel direct feedthrough (Fig. 5c). The coil body was designed with Solidworks (SolidWorks Corp., MA, USA) and 3D printed (3D Systems, Inc., SC, USA), and wound with 24 AWG-equivalent Litz wire (MWS Wire Industries, CA, USA). The receiver coils were connected to custom bandstop filters to minimize direct feedthrough interference before signal amplification with a custom preamplifier and digitization.

C. Phantom Construction

To validate the resolution improvement from combined multichannel MPI imaging, we constructed three different imaging phantoms, all were laser engraved out of an acrylic plate.

First, we constructed a “Cal” phantom (Fig. 1), which has approximately 2 mm uniform channel width throughout the phantom. The channels were then injected with undiluted Micromod nanomag-MIP particles (micromod Partikeltechnologie GmbH, Germany).

We also constructed a resolution phantom (Fig. 6a) with 6 evenly distributed groups of channels around the circumference of the phantom. Within each group, the channels are separated by a controlled distance ranging from 3 mm to 0.5 mm. We then injected the channels with 5× diluted Micromod nanomag-MIP particles and sealed the channels with clear nail polish.

D. MPI Experimental Scanning Parameters and Image Reconstruction

MPI experiments were performed using linear drive field trajectories. In each set of experiments, we acquired two orthogonal collinear scans. In each scan, the FFP is excited sinusoidally in either y or z axis with the corresponding RF coil to create a pFOV [37]. Both channels have RF excitation field strengths of 30 mTpp at 20.05 kHz excitation frequency. The pFOV is then rastered with a Cartesian trajectory across the entire imaging FOV, as seen in Fig. 5d. Mechanical movement of the sample occurs in the z axis with 67% pFOV overlap.

For the “Cal” phantom, the imaging FOV for collinear y scan is 2 by 4.1 by 10 cm along the x, y and z axis respectively. The scan time was 7.5 min. The imaging FOV for collinear z scan is 2 by 4.5 by 9.9 cm, with a scan time of 2 min.

For the resolution phantom, the imaging FOVs for both channels were 2 by 4.5 by 5 cm, with a y scan time of 3.75 min, and z scan time of 1 min.

To reconstruct isotropic x-space MPI images, we first reconstruct each collinear channel image separately using x-space reconstruction [37], [39]. Following the algorithm presented in Eq. 13, we then normalize each reconstructed MPI image by the receive coil sensitivity,

Author Manuscript Author Manuscript Author Manuscript Author Manuscript

interpolated each image onto the same image-domain sampling density, and summed the images to form a composite isotropic-resolution image.

IV. Results

A. Multi-channel MPI hardware specifications

An image of the constructed multi-channel MPI drive and detector coils is shown in Figure 5 (b) and (c). The drive field coils were able to produce 40 mTpp field using 1.6 kW and 2.7 kW in the axial and transverse directions, respectively. This corresponds a total pFOV size of 11.4 mm along the drive field direction [37]. Combined with additional high-inductance electromagnets along the the scanner's x- and y- cardinal directions (not shown), the scanner has a maximum x-y plane FOV of 4×4cm. The z-axis FOV can be arbitrarily long for typical scans, as the animal is translated relative to the FFR via the use of a robot stage along the z-axis akin to computed tomography techniques.

The sensitivity of the axial and transverse detector coils is 860 μT/A and 420 μT/A respectively. For multi-channel imaging, reconstructed images for each drive channel were normalized in amplitude by the detector coil sensitivity prior to reconstructing isotropic-resolution MPI images.

B. Experimental verification of isotropic MPI spatial resolution

We used the multi-channel FFP MPI system to scan SPIO imaging phantoms to test our algorithm for achieving isotropic spatial resolution (Figs. 1 and 6). Figure 1 shows an acrylic "Cal" phantom with laser-cut channels filled with SPIO tracer. Single-channel MPI images acquired in the y- and z-directions showed anisotropic resolution and signal dropouts along segments of the channel parallel to the drive field direction. This is consistent with descriptions of the single-channel MPI PSF in literature [39] as well as our theory and simulations in Figs. 2 and 4, where the normal component of the PSF, which is shown to have poor spatial resolution, is orthogonal to the drive field direction. After normalizing the respective singlechannel images by the gradient strength and the detector coil sensitivity, the combined image in Fig. 1 d shows isotropic resolution and recovery of the image intensity dropouts along the channel.

Fig. 6 shows a resolution phantom filled with SPIO tracer, with channel width and channel separation distance both ranging from 0.5 mm to 3 mm. Subfigures b and c show the two orthogonal collinear scans in the horizontal and vertical directions respectively, both showing anisotropic resolution. In the y-channel scan (Fig. 6b), the 1 mm and 1.5 mm separation distance channels are distinguishable within the reconstructed image, though the 2 mm channels are indistinguishable, because of the poor spatial resolution along the z-axis. In the z-channel scan (Fig. 6c), the 2 mm channels are clearly distinguishable, but the image suffers from increased blurring along the y-direction. After normalizing the two scans and combining them, the result shown in Fig. 6d shows isotropic resolution. Specifically, all phantom channels down to 1.5 mm are distinguishable regardless of their rotational orientation within the FOV.

Author Manuscript Author Manuscript Author Manuscript Author Manuscript

V. Discussion

In this work, we identified the source of image anisotropy in Magnetic Particle Imaging by decomposing the MPI PSF into tangential and normal envelopes that are anisotropically weighted depending on image acquisition trajectory parameters. Using this analytical framework, we then demonstrated mathematically and experimentally that isotropic spatial resolution in MPI can be made achieved via the use of combined orthogonal multi-channel scans. This algorithm is simple, well-conditioned, and only requires the addition of orthogonal MPI drive and detector coils. Further, our algorithm does not operate on the raw MPI time-signal, but operates on the images after they are reconstructed. Hence, system timing delays arising from propagation delays in the DAQ, amplifier, filters, or phase offsets in the reactance of the transmitter are already calibrated for image reconstruction and do not affect the multi-channel isotropicity algorithm. Below we discuss the implications of this work on future work in MPI theory, scanning trajectories, and scanner design.

A. Implications of E_T and E_N on spatial resolution

Here we described in detail two competing mechanisms that produce signal in MPI: SPIO magnetization and demagnetization following the Langevin curve (E_T) and the rotation of the magnetic moment to align with the applied field (E_N). For improved spatial resolution, it would be desirable to acquire only the higher-resolution E_T signal component. However, we demonstrated here that the received signal is comprised of a mixture of these two mechanisms acquired simultaneously, and is present for any combination of drive field trajectories and detector coil orientations (i.e. any component of the image tensor $\mathbf{\Omega}(x)$). This implies that simple signal processing techniques (e.g. scanning trajectories, analog filtering, or time domain digital filters) cannot separate these two physical processes from each other. The algorithm presented here results in a PSF which is comprised of a mixture of both the tangential and normal envelopes (Eqn. 13), with a FWHM resolution between that of the two envelopes. While it is possible to sharpen the images via the use of nonlinear operations like multiplication and logarithms, these would cause the MPI images to lose their LSI properties. However, it may be possible to characterize and compensate for the excessive low-frequency signal components in the PSF arising from E_N via the use of a density-compensating equalization filter, similar to the filtered backprojection method used in CT imaging.

We note here we have assumed an adiabatic SPIO response, whereby the particle response is instantaneous to the applied field and has been shown to be accurate for many formulations of SPIOs and MPI scanning parameters [11], [39]. However, as magnetic relaxation effects increase for varying SPIO particles (of larger core diameters, for example), MPI image resolution and signal-noise ratio (SNR) can suffer significantly [31].

B. Implications of MPI imaging tensor for scanning trajectory design

Here we demonstrated that the MPI signal is acquired and modulated by probing a multidimensional MPI image tensor using different combinations of drive field trajectories and receiver coil configurations. This tensor-based understanding of the PSF may lead to future improvements in spatial resolution and scanning speed. Specifically, we showed that

Author Manuscript Author Manuscript Author Manuscript Author Manuscript

combining orthogonal Cartesian drive field trajectories is sufficient for achieving isotropic resolution. But this scanning scheme requires multiple x-space temporal acquisitions with orthogonal scanning channels. Other imaging trajectories are also possible and may increase scanning speed, but our analysis in Eqns. 17 and 18 suggest that x-space isotropic resolution is only achievable for combinations of trajectories which can orthogonally sample each point in x-space. Moreover, we note that our algorithm holds for trajectories where the drive field direction and detector coil orientation are collinear. For dynamically changing drive field trajectories, a temporally-weighted combination of signals from orthogonal detector coils might suffice for this purpose.

Another implication of the tensor analysis MPI signals is in the potential utility of the off-diagonal image tensor components in Eqn. 10. We showed in Fig. 2 that the off-diagonal tensor PSF contains modified weighting matrices and both positive and negative image signal components. While it is uncertain whether such off-diagonal tensor images may be useful in improving spatial resolution, which is a topic that merits further analysis, one application of these images could be to improve image SNR by enforcing data consistency as part of the forward model used in optimized image reconstructions [51].

The algorithm proposed here may also be readily adapted to other MPI techniques, such as slice-scanning mode traveling-wave MPI [52], provided that orthogonal collinear image tensor components $\hat{\rho}_{ii}(\mathbf{x})$ are fully sampled during signal acquisition.

C. Advantages of FFL MPI designs

Here we show MPI scans using FFL magnetic gradients, where $\mathbf{G} = \begin{bmatrix} G & 0 & 0 \\ 0 & 0 & 0 \\ 0 & 0 & -G \end{bmatrix}$ for example, have an inherent advantage over FFP scanners in resolution, along with their established advantages in SNR and imaging speed. It has been previously shown that FFL-based MPI scanners, which form project images that integrate all SPIO signal along the axis of the FFL, can achieve up to an order-of-magnitude faster imaging speed from 3D FFP scans [18]. FFL-based projection scans can be rotated to form a 3D image using algorithms like filtered backprojection, akin to CT reconstructions, which result in order-of-magnitude improvements in SNR over FFP 3D scans along with higher radial image resolution [16], [19], [53].

Further, Maxwell's equations dictate that the FFP scanner gradient field must be higher in one dimension (the x-axis, in our setup) than the other two dimensions. Hence, our algorithm, applied to 3-channel orthogonal MPI scans, would result in a PSF that are isotropic in the yz-plane but with improved FWHM resolution along the x-axis, forming a well-behaved, oblate spheroid shaped-PSF in 3D. In contrast, for FFL scanners, our multi-channel algorithm results in well-behaved isotropic PSFs, since the magnetic gradient is zero along the FFL direction. Finally, the use of FFL MPI imaging with our algorithm enables a higher-resolution image than an FFP scanner, owing to the result that the projection FFL PSF contains only one part of the low-resolution E_N component (Eqn. 14), compared to two parts for a FFP scanner (Eqn. 13). These attributes, combined with the improved sensitivity,

Author Manuscript Author Manuscript Author Manuscript Author Manuscript

speed, and radial resolution already described for FFL images, may make FFL MPI designs more advantageous than FFP scanners for clinical applications.

VI. Conclusion

In this work we showed that MPI images are acquired by probing an image tensor using specific drive field and detector scanning trajectories. Using this analysis, we proved and experimentally demonstrated that we can reshape the MPI PSF to be isotropic and well-behaved with multi-channel acquisition, enabling improved MPI resolution and opportunities for optimizing MPI trajectory design.

Acknowledgment

We are grateful for funding support from UC Discovery Grant 29623, NIH 5R01EB013689, CIRM RT2-01893, Keck Foundation Grant 009323, NIH 1R24MH106053, and NIH 1R01EB019458. K. Lu was supported by the CIRM Scholars program, and B. Zheng was supported by the Siebel Scholars program.

Appendix

A. Proof of isotropic resolution via combined orthogonal collinear scans

In this section, we will prove that by combining three orthogonal collinear scans for FFP MPI scanners, we can achieve isotropic MPI resolution. As shown in Eq. 13, the analytic expression of the combined three orthogonal collinear scans is

$$\begin{aligned}\hat{\rho}(\vec{\mathbf{x}}) &= \mathrm{trace}[\mathbf{\Omega}(\vec{\mathbf{x}})\mathbf{G}^{-1}] \\ &= \sum_{i=1}^{3} \hat{\mathbf{e}}_{\mathbf{i}}^{\mathbf{T}}\mathbf{\Omega}(\vec{\mathbf{x}})\mathbf{G}^{-1}\hat{\mathbf{e}}_{\mathbf{i}}\end{aligned} \quad (15)$$

$$= \rho(\vec{\mathbf{x}}) * * * \sum_{i=1}^{3} \hat{\mathbf{e}}_{\mathbf{i}}^{\mathbf{T}}\mathbf{h}(\vec{\mathbf{x}})\mathbf{G}^{-1}\hat{\mathbf{e}}_{\mathbf{i}} \quad (16)$$

Let us denote the unit vector $\frac{\mathbf{G}\vec{\mathbf{x}}}{\|\mathbf{G}\vec{\mathbf{x}}\|}$ as $\vec{\mathbf{r}}(\vec{\mathbf{x}})$, thus $\mathbf{W}_T(\vec{\mathbf{x}}) = \vec{\mathbf{r}}(\vec{\mathbf{x}})\vec{\mathbf{r}}(\vec{\mathbf{x}})^{\mathbf{T}}\mathbf{G}$, and $\mathbf{W}_N(\vec{\mathbf{x}}) = \mathbf{G} - \mathbf{W}_T(\vec{\mathbf{x}})$. Thus

$$\begin{aligned}\hat{\rho}(\vec{\mathbf{x}}) = \rho(\vec{\mathbf{x}}) * * * \Bigg(& E_T(\vec{\mathbf{x}}) \sum_{i=1}^{3} \hat{\mathbf{e}}_{\mathbf{i}}^{\mathbf{T}}\vec{\mathbf{r}}(\vec{\mathbf{x}})\vec{\mathbf{r}}(\vec{\mathbf{x}})^{\mathbf{T}}\hat{\mathbf{e}}_{\mathbf{i}} \\ & + E_N(\vec{\mathbf{x}})\left[3 - \sum_{i=1}^{3} \hat{\mathbf{e}}_{\mathbf{i}}^{\mathbf{T}}\vec{\mathbf{r}}(\vec{\mathbf{x}})\vec{\mathbf{r}}(\vec{\mathbf{x}})^{\mathbf{T}}\hat{\mathbf{e}}_{\mathbf{i}}\right]\Bigg)\end{aligned} \quad (17)$$

Author Manuscript Author Manuscript Author Manuscript Author Manuscript

As has been shown, the two envelopes $E_T(\vec{\mathbf{x}})$ and $E_N(\vec{\mathbf{x}})$ are isotropic. Therefore, for the entire equation to remain isotropic, it hinges on the isotropy of $\sum_{i=1}^{3}\hat{\mathbf{e}}_\mathbf{i}^\mathbf{T}\vec{\mathbf{r}}(\vec{\mathbf{x}})\vec{\mathbf{r}}(\vec{\mathbf{x}})^\mathbf{T}\hat{\mathbf{e}}_\mathbf{i}$. It can be proven that the sum is merely a constant value, and is thus spatially invariant:

$$\begin{aligned}\sum_{i=1}^{3}\hat{\mathbf{e}}_\mathbf{i}^\mathbf{T}\vec{\mathbf{r}}(\vec{\mathbf{x}})\vec{\mathbf{r}}(\vec{\mathbf{x}})^\mathbf{T}\hat{\mathbf{e}}_\mathbf{i} &= \sum_{i=1}^{3}\vec{\mathbf{r}}(\vec{\mathbf{x}})^\mathbf{T}\hat{\mathbf{e}}_\mathbf{i}\hat{\mathbf{e}}_\mathbf{i}^\mathbf{T}\vec{\mathbf{r}}(\vec{\mathbf{x}}) \\ &= \vec{\mathbf{r}}(\vec{\mathbf{x}})^\mathbf{T}\left(\sum_{i=1}^{3}\hat{\mathbf{e}}_\mathbf{i}\hat{\mathbf{e}}_\mathbf{i}^\mathbf{T}\right)\vec{\mathbf{r}}(\vec{\mathbf{x}}) \\ &= \vec{\mathbf{r}}(\vec{\mathbf{x}})^\mathbf{T}\mathbf{I}\vec{\mathbf{r}}(\vec{\mathbf{x}}) = 1\end{aligned} \tag{18}$$

where we make the substitution of $\sum_{i=1}^{3}\left(\hat{\mathbf{e}}_i\hat{\mathbf{e}}_i^\mathbf{T}\right) = [\ \hat{\mathbf{e}}_1\ \ \hat{\mathbf{e}}_2\ \ \hat{\mathbf{e}}_3]\begin{bmatrix}\hat{\mathbf{e}}_1^\mathbf{T}\\ \hat{\mathbf{e}}_2^\mathbf{T}\\ \hat{\mathbf{e}}_3^\mathbf{T}\end{bmatrix}$, and apply the orthogonal matrix identity $AA^T = I$, as $A = [\ \hat{\mathbf{e}}_1\ \ \hat{\mathbf{e}}_2\ \ \hat{\mathbf{e}}_3]$ is chosen to be orthogonal during scanning. If we plug Eq. 18 into Eq. 17, we arrive at the conclusion that

$$\hat{\rho}(\vec{\mathbf{x}}) = \rho(\vec{\mathbf{x}}) * * * (E_T(\vec{\mathbf{x}}) + 2E_N(\vec{\mathbf{x}})) \tag{19}$$

Hence, the anisotropy from the weighting matrix $\mathbf{W}_T(\vec{\mathbf{x}})$ and $\mathbf{W}_N(\vec{\mathbf{x}})$ are removed after weighted summation of three orthogonal MPI scans.

References

[1]. Gleich B and Weizenecker J, “Tomographic imaging using the nonlinear response of magnetic particles”, Nature, vol. 435, no. 7046, pp. 1214–1217, Jun. 2005. [PubMed: 15988521]

[2]. Pankhurst QA, Connolly J, Jones SK, and Dobson J, “Applications of magnetic nanoparticles in biomedicine”, J. Phys. D Appl. Phys, vol. 36, no. 13, R167, 2003.

[3]. LaConte L, Nitin N, and Bao G, “Magnetic nanoparticle probes”, Mater. Today, vol. 8, no. 5, Supplement 1, pp. 32–38, 5 2005.

[4]. Neuwelt E. a., Hamilton BE, Varallyay CG, Rooney WR, Edelman RD, Jacobs PM, and Watnick SG, “Ultrasmall superparamagnetic iron oxides (US- PlOs): A future alternative magnetic resonance (MR) contrast agent for patients at risk for nephrogenic systemic fibrosis (NSF)?” Kidney Int., vol. 75, no. 5, pp. 465–474, Mar. 2009. [PubMed: 18843256]

[5]. Zheng B, Vazin T, Goodwill PW, Conway A, Verma A, Ulku Saritas E, Schaffer D, and Conolly SM, “Magnetic particle imaging tracks the long-term fate of in vivo neural cell implants with high image contrast”, Sci. Rep, vol. 5, p. 14055, Sep. 2015. [PubMed: 26358296]

[6]. Zheng B, von See MP, Yu E, Gunel B, Lu K, Vazin T, Schaffer DV, Goodwill PW, and Conolly SM, “Quantitative magnetic particle imaging monitors the transplantation, biodistribution, and clearance of stem cells in vivo”, Theranostics, vol. 6, no. 3, pp. 291–301, Jan. 2016. [PubMed: 26909106]

[7]. Saritas EU, Goodwill PW, Croft LR, Konkle JJ, Lu K, Zheng B, and Conolly SM, “Magnetic particle imaging (MPI) for NMR and MRI researchers,” J. Magn. Reson, vol. 229, pp. 116–126, Apr. 2013. [PubMed: 23305842]

Author Manuscript Author Manuscript Author Manuscript Author Manuscript

[8]. Weizenecker J, Borgert J, and Gleich B, “A simulation study on the resolution and sensitivity of magnetic particle imaging”, Phys. Med. Biol, vol. 52, no. 21, pp. 6363–6374, Nov. 2007. [PubMed: 17951848]

[9]. Lu M, Cohen MH, Rieves D, and Pazdur R, “FDA report: Ferumoxytol for intravenous iron therapy in adult patients with chronic kidney disease”, Am. J. Hematol, vol. 85, no. 5, pp. 315–319, 5 2010. [PubMed: 20201089]

[10]. Weissleder R, Stark DD, Engelstad BL, Bacon BR, Compton CC, White DL, Jacobs P, and Lewis J, “Superparamagnetic iron oxide: Pharmacokinetics and toxicity”, AJR Am. J. Roentgenol, vol. 152, no. 1, pp. 167–173, Jan. 1989. [PubMed: 2783272]

[11]. Goodwill PW, Saritas EU, Croft LR, Kim TN, Krishnan KM, Schaffer DV, and Conolly SM, “X-space MPI: Magnetic nanoparticles for safe medical imaging”, Adv. Mater, vol. 24, no. 28, pp. 3870–3877, Jul. 2012. [PubMed: 22988557]

[12]. Borgert J, Schmidt JD, Schmale I, Rahmer J, Bontus C, Gleich B, David B, Eckart R, Woywode O, Weizenecker J, Schnorr J, Taupitz M, Haegele J, Vogt BM, and Barkhausen J, “Fundamentals and applications of magnetic particle imaging”, J. Cardiovasc. Comput. Tomogr, vol. 6, no. 3, pp. 149–153, 5 2012. [PubMed: 22682260]

[13]. Rahmer J, Antonelli A, Sfara C, Tiemann B, Gleich B, Magnani M, Weizenecker J, and Borgert J, “Nanoparticle encapsulation in red blood cells enables blood-pool magnetic particle imaging hours after injection”, Phys. Med. Biol, vol. 58, no. 12, pp. 3965–3977, Jun. 2013. [PubMed: 23685712]

[14]. Bulte JWM, Walczak P, Janowski M, Krishnan KM, Arami H, Halkola A, Gleich B, and Rahmer J, “Quantitative “hot spot” imaging of transplanted stem cells using superparamagnetic tracers and magnetic particle imaging (MPI)”, Tomography, vol. 1, no. 2, pp. 91–97, Dec. 2015. [PubMed: 26740972]

[15]. Yu EY, Bishop M, Zheng B, Ferguson RM, Khandhar AP, Kemp SJ, Krishnan KM, Goodwill PW, and Conolly SM, “Magnetic particle imaging: A novel in vivo imaging platform for cancer detection”, Nano Lett., vol. 17, no. 3, pp. 1648–1654, Feb. 2017. [PubMed: 28206771]

[16]. Weizenecker J, Gleich B, and Borgert J, “Magnetic particle imaging using a field free line”, J. Phys. D Appl. Phys, vol. 41, no. 10, p. 105 009, 5 2008.

[17]. Erbe M, Knopp T, Sattel TF, Biederer S, and Buzug TM, “Experimental generation of an arbitrarily rotated field-free line for the use in magnetic particle imaging”, Med. Phys, vol. 38, no. 9, pp. 5200–5207, Sep. 2011. [PubMed: 21978064]

[18]. Goodwill PW, Konkle JJ, Zheng B, Saritas EU, and Conolly SM, “Projection x-space magnetic particle imaging”, IEEE Trans. Med. Imaging, vol. 31, no. 5, pp. 1076–1085, 5 2012. [PubMed: 22552332]

[19]. Konkle JJ, Goodwill PW, Carrasco-Zevallos OM, and Conolly SM, “Projection reconstruction magnetic particle imaging”, IEEE Trans. Med. Imaging, vol. 32, no. 2, pp. 338–347, Feb. 2013. [PubMed: 23193308]

[20]. Goodwill PW, Lu K, Zheng B, and Conolly SM, “An x-space magnetic particle imaging scanner”, Rev. Sci. Instrum, vol. 83, no. 3, p. 033 708, Mar. 2012.

[21]. Sattel TF, Knopp T, Biederer S, Gleich B, Weizenecker J, Borgert J, and Buzug TM, “Singlesided device for magnetic particle imaging”, J. Phys. D Appl. Phys, vol. 42, p. 022001, 2008.

[22]. Haegele J, Rahmer J, Gleich B, Borgert J, Wojtczyk H, Panagiotopoulos N, Buzug TM, Barkhausen J, and Vogt FM, “Magnetic particle imaging: Visualization of instruments for cardiovascular intervention”, Radiology, vol. 265, no. 3, pp. 933–938, Dec. 2012. [PubMed: 22996744]

[23]. Haegele J, Biederer S, Wojtczyk H, Gräser M, Knopp T, Buzug TM, Barkhausen J, and Vogt FM, “Toward cardiovascular interventions guided by magnetic particle imaging: First instrument characterization”, Magn. Reson. Med, vol. 69, no. 6, pp. 1761–1767, Jun. 2013. [PubMed: 22829518]

[24]. Vogel P, Ruckert MA, Klauer P, Kullmann WH, Jakob PM, and Behr VC, “Traveling wave magnetic particle imaging”, IEEE Trans. Med. Imaging, vol. 33, no. 2, pp. 400–407, Feb. 2014. [PubMed: 24132006]

Author Manuscript Author Manuscript Author Manuscript Author Manuscript

[25]. Ferguson RM, Minard KR, and Krishnan KM, “Optimization of nanoparticle core size for magnetic particle imaging”, J. Magn. Magn. Mater, vol. 321, pp. 1548–1551, 2009. [PubMed: 19606261]

[26]. Ferguson RM, Minard KR, Khandhar AP, and Krishnan KM, “Optimizing magnetite nanoparticles for mass sensitivity in magnetic particle imaging”, Med. Phys, vol. 38, no. 3, p. 1619, 2011. [PubMed: 21520874]

[27]. Ferguson RM, Khandhar AP, and Krishnan KM, “Tracer design for magnetic particle imaging (invited)”, J. Appl. Phys, vol. 111, no. 7, 7B318–7B3185, Apr. 2012.

[28]. Croft LR, Goodwill PW, and Conolly SM, “Relaxation in x-space magnetic particle imaging”, IEEE Trans. Med. Imaging, vol. 31, no. 12, pp. 2335–2342, Dec. 2012. [PubMed: 22968211]

[29]. Martens MA, Deissler RJ, Wu Y, Bauer L, Yao Z, Brown R, and Griswold M, “Modeling the brownian relaxation of nanoparticle ferrofluids: Comparison with experiment”, Med. Phys, vol. 40, no. 2, p. 022 303, Feb. 2013.

[30]. Weaver JB, Zhang X, Kuehlert E, Toraya-Brown S, Reeves B, Perreard IM, and Fiering S, “Quantification of magnetic nanoparticles with low frequency magnetic fields: Compensating for relaxation effects”, Nanotechnology, vol. 24, no. 32, p. 325 502, Aug. 2013.

[31]. Tay ZW, Hensley DW, Vreeland EC, Zheng B, and Conolly SM, “The relaxation wall: Experimental limits to improving MPI spatial resolution by increasing nanoparticle core size”, Biomed. Phys. Eng. Express, vol. 3, no. 3, p. 035003, Apr. 2017. [PubMed: 29250434]

[32]. Rahmer J, Weizenecker J, Gleich B, and Borgert J, “Signal encoding in magnetic particle imaging: Properties of the system function”, BMC Med. Imaging, vol. 9, p. 4, Jan. 2009. [PubMed: 19335923]

[33]. Rahmer J, Halkola A, Gleich B, Schmale I, and Borgert J, “First experimental evidence of the feasibility of multi-color magnetic particle imaging”, Phys. Med. Biol, vol. 60, no. 5, pp. 1775–1791, Mar. 2015. [PubMed: 25658130]

[34]. Rahmer J, Weizenecker J, Gleich B, and Borgert J, “Analysis of a 3-D system function measured for magnetic particle imaging”, IEEE Trans. Med. Imaging, vol. 31, no. 6, pp. 1289–1299, Jun. 2012. [PubMed: 22361663]

[35]. Knopp T, Rahmer J, Sattel TF, Biederer S, Weizenecker J, Gleich B, Borgert J, and Buzug TM, “Weighted iterative reconstruction for magnetic particle imaging”, Phys. Med. Biol, vol. 55, pp. 1577–1589, 2010. [PubMed: 20164532]

[36]. Knopp T, Sattel TF, Biederer S, Rahmer J, Weizenecker J, Gleich B, Borgert J, and Buzug TM, “Modelbased reconstruction for magnetic particle imaging”, IEEE Trans. Med. Imaging, vol. 29, no. 1, pp. 12–18, Jan. 2010. [PubMed: 19435678]

[37]. Lu K, Goodwill PW, Saritas EU, Zheng B, and Conolly SM, “Linearity and shift invariance for quantitative magnetic particle imaging”, IEEE Trans. Med. Imaging, vol. 32, no. 9, pp. 1565–1575, Sep. 2013. [PubMed: 23568496]

[38]. Goodwill PW and Conolly SM, “The x-space formulation of the magnetic particle imaging process: 1-D signal, resolution, bandwidth, SNR, SAR, and magnetostimulation”, IEEE Trans. Med. Imaging, vol. 29, no. 11, pp. 1851–1859, Nov. 2010. [PubMed: 20529726]

[39]. Goodwill PW and Conolly SM, “Multidimensional X-Space magnetic particle imaging”, IEEE Trans. Med. Imaging, vol. 30, no. 9, pp. 1581–1590, Sep. 2011. [PubMed: 21402508]

[40]. Vogel P, Ruckert MA, Klauer P, Kullmann WH, Jakob PM, and Behr VC, “First in vivo traveling wave magnetic particle imaging of a beating mouse heart”, Phys. Med. Biol, vol. 61, no. 18, pp. 6620–6634, Aug. 2016. [PubMed: 27541258]

[41]. Vogel P, Rückert MA, Klauer P, Herz S, Kampf T, Bley T, and Behr VC, “Real-time 3D dynamic rotating Slice-Scanning mode for traveling wave MPI”, International Journal on Magnetic Particle Imaging, vol. 3, no. 2, pp. 1–7, Jun. 2017.

[42]. Saritas EU, Goodwill PW, Zhang GZ, and Conolly SM, “Magnetostimulation limits in magnetic particle imaging”, IEEE Trans. Med. Imaging, vol. 32, no. 9, pp. 1600–1610, Sep. 2013. [PubMed: 23649181]

[43]. Saritas EU, Goodwill PW, and Conolly SM, “Effects of pulse duration on magnetostimulation thresholds”, Med. Phys, vol. 42, no. 6, pp. 3005–3012, Jun. 2015. [PubMed: 26127053]

Author Manuscript Author Manuscript Author Manuscript Author Manuscript

[44]. Vogel P, Kampf T, Rückert MA, and Behr VC, “Flexible and dynamic patch reconstruction for traveling wave magnetic particle imaging”, International Journal on Magnetic Particle Imaging, vol. 2, no. 2, Nov. 2016.

[45]. Ferguson RM, Khandhar AP, Kemp SJ, Arami H, Saritas U, Croft LR, Konkle J, Goodwill PW, Halkola A, Rahmer J, Borgert J, Conolly SM, and Krishnan KM, “Magnetic particle imaging with tailored iron oxide nanoparticle tracers”, IEEE Trans. Med. Imaging, vol. 34, no. 5, pp. 1077–1084, 5 2015. [PubMed: 25438306]

[46]. Knopp T, Biederer S, Sattel T, Weizenecker J, Gleich B, Borgert J, and Buzug TM, “Trajectory analysis for magnetic particle imaging”, Phys. Med. Biol, vol. 54, pp. 385–397, 2009. [PubMed: 19098358]

[47]. Vogel P, Ruckert MA, Jakob PM, and Behr VC, “microMPI – initial experiments with an ultrahigh resolution MPI”, IEEE Trans. Magn, vol. 51, no. 2, pp. 1–4, Feb. 2015. [PubMed: 26203196]

[48]. Vogel P, Ruckert MA, Kemp SJ, Khandhar AP, Ferguson RM, Vilter A, Klauer P, Krishnan KM, and Behr VC, “Micro traveling wave MPI – initial results with optimized tracer LS-008,” in International Workshop on Magnetic Particle Imaging, Lvbeck, Germany, Mar. 2016, p. 138.

[49]. Panagiotopoulos N, Duschka RL, Ahlborg M, Bringout G, Debbeler C, Graeser M, Kaethner C, Ludtke-Buzug K, Medimagh H, Stelzner J, Buzug TM, Barkhausen J, Vogt FM, and Haegele J, “Magnetic particle imaging: Current developments and future directions”, Int. J. Nanomedicine, vol. 10, pp. 3097–3114, Apr. 2015. [PubMed: 25960650]

[50]. Goodwill P, Croft L, Konkle J, Lu K, Saritas E, Zheng B, and Conolly S, “Third generation X-Space MPI mouse and rat scanner,” in Magnetic Particle Imaging, ser. Springer Proceedings in Physics, Springer Berlin Heidelberg, 2012, pp. 261–265.

[51]. Konkle JJ, Goodwill PW, Hensley DW, Orendorff RD, Lustig M, and Conolly SM, “A convex formulation for magnetic particle imaging X-Space reconstruction”, PLoS One, vol. 10, no. 10, e0140137, Oct. 2015. [PubMed: 26495839]

[52]. Vogel P, Ruckert M, Klauer P, Kullmann W, Jakob P, and Behr V, “Slicing frequency mixed traveling wave for 3d magnetic particle imaging,” in Magnetic Particle Imaging, Springer, 2012, pp. 231–235.

[53]. Konkle JJ, Goodwill PW, Saritas EU, Zheng B, Lu K, and Conolly SM, “Twenty-fold acceleration of 3D projection reconstruction MPI”, Biomed. Tech, vol. 58, no. 6, pp. 565–576, Dec. 2013.

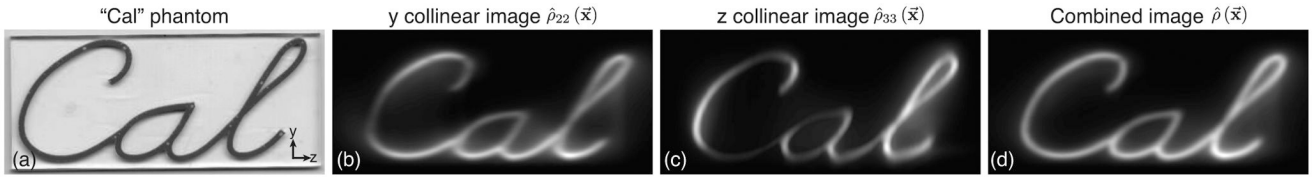

Fig. 1.

Isotropic MPI native resolution is enabled via a simple algorithm combining multi-channel image acquisitions. Experimental MPI imaging data acquired on a 7×3.5×3.5 T/m MPI scanner. (a) Photograph of a "Cal" shaped acrylic phantom injected with Micromod Nanomag-MIP particles (10.6μg/mL). (b) Collinear scan acquired with a single y channel, showing anisotropic resolution. The horizontal haze is due to the slow signal decay perpendicular to excitation direction, and this haze blurs image and reduces its contrast. Imaging FOV: 2×4.1×10cm respectively along the x, y, and z axes. 7.5 min acquisition time. (c) Collinear scan acquired with single z channel. Imaging FOV: 2×4.5×9.9 cm respectively along the x, y, and z axes. 2 min acquisition time. (d) Combining two orthogonal collinear scans from (b) and (c) achieves planar isotropic resolution.

Author Manuscript
Author Manuscript
Author Manuscript
Author Manuscript

Author Manuscript Author Manuscript Author Manuscript Author Manuscript

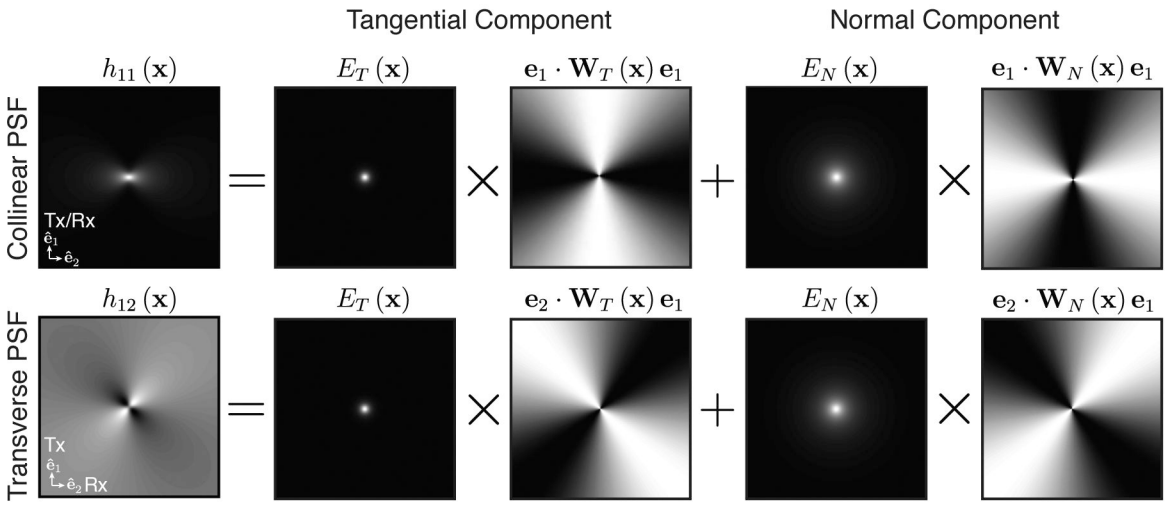

Fig. 2.

Decomposition of collinear (top) and transverse (bottom) MPI PSFs, assuming spatially homogeneous receiver coil sensitivities. Each PSF is the sum of tangential and normal components, which are the multiplication of a radially symmetric envelope (E_T(x) and E_N(x)) by a spatially asymmetric weighting matrix (W_T(x) and W_T(x)), projected onto the drive/receiver trajectories (respectively e_1 and e_2 for the collinear PSF, e_1 and e_2 for the the transverse PSF). These non-isotropic weighting matrices cause the native MPI PSF to be rotationally anisotropic. Importantly, the transverse PSF contains positive and negative components, because the projection of the weighting matrices W_T(x) and W_N(x) onto the drive/receiver trajectories e_1 and e_2 ranges from negative to positive values.

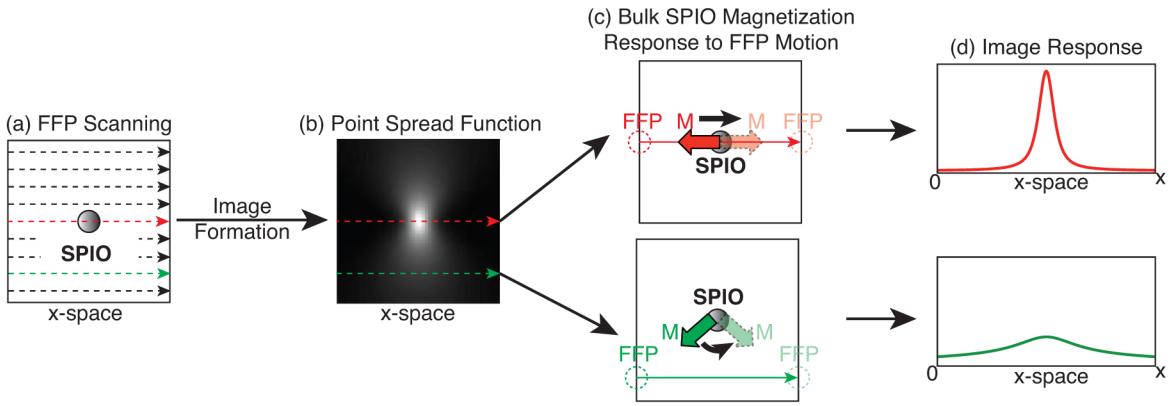

Fig. 3.

Physical mechanism MPI image anisotropy. (a) A SPIO point source scanned with a linear FFR trajectory gives an anisotropic PSF (b). (c) Two methods for bulk SPIO magnetization response to FFR movement: (top) the SPIO magnetization magnitude changes rapidly and intensely following Langevin physics, xor (bottom) SPIO magnetization magnitude remains unchanged, but slowly rotates to align with the instantaneous FFR location [32], [39]. These mechanisms yield signals with significantly different amplitudes and extent in both the received signal and the MPI image, show in (d).

Author Manuscript
Author Manuscript
Author Manuscript
Author Manuscript

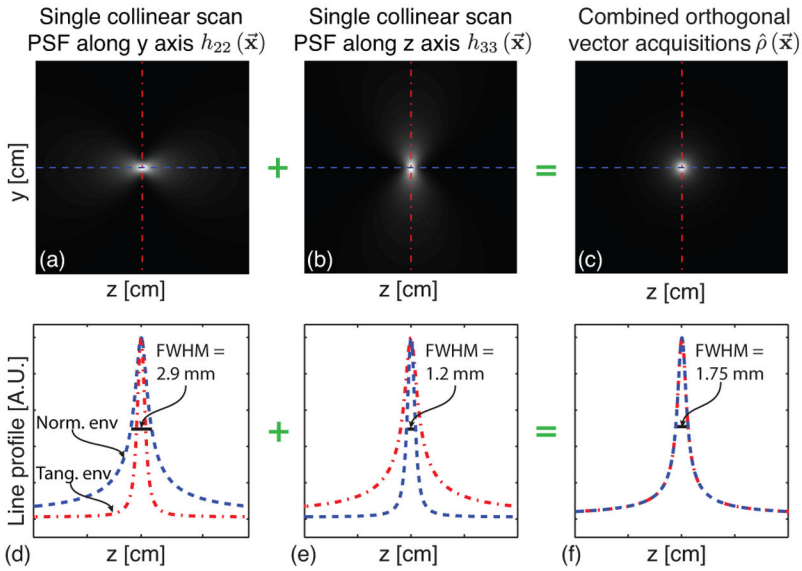

Fig. 4.

[Top] Two summed orthogonal collinear scans are sufficient to remove anisotropy from MPI PSF arising from weighting matrices. The resulting PSF is the average between the tangential and normal PSF envelopes. (a-b) *Ab initio* simulations show yz cross-sectional images respectively of y- and z- axis collinear scans. (c) Combined orthogonal collinear PSF yields isotropic resolution in yz plane. Three orthogonal collinear scans is sufficient for 3D isotropic resolution for isotropic gradient fields. For Maxwell pair gradient fields, summed three orthogonal collinear scans yields a PSF with a well-behaved oblate spheroid shape. [Bottom] Line profile of respective PSFs. The resolution of the averaged collinear PSF is between that of the tangential and normal envelopes.

Author Manuscript Author Manuscript Author Manuscript Author Manuscript

Author Manuscript

Author Manuscript

Author Manuscript

Author Manuscript

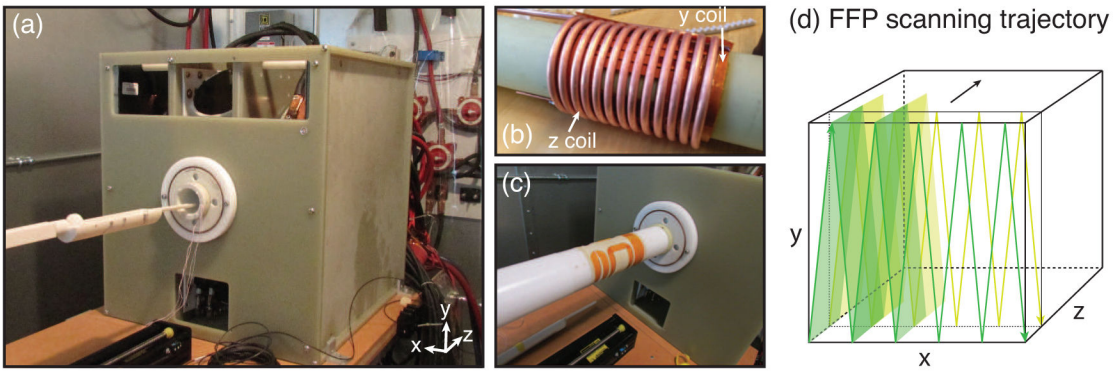

Fig. 5.

Photos of multi-channel MPI hardware. (a) Gertrude 7 T/m FFP scanner developed at UC Berkeley. (b) Customized transmit coil assembly with a water-cooled solenoid coil for generating axial RF field and a double-layered Golay coil pair for generating transverse RF field. (c) Customized receive coil assembly with an axial and transverse receive coil respectively. (d) Example FFP trajectory used to acquire collinear z-axis images.

Author Manuscript Author Manuscript Author Manuscript Author Manuscript

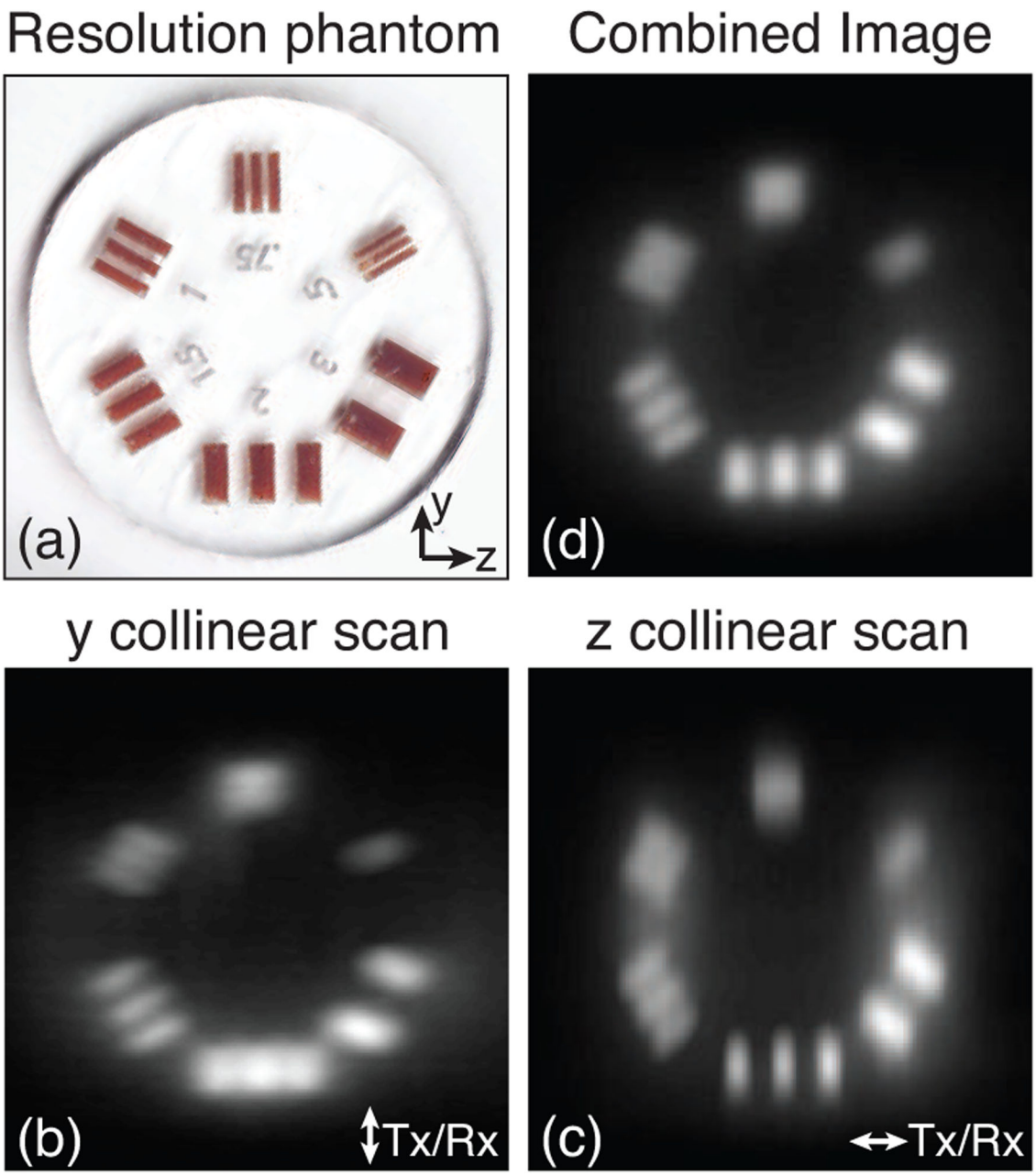

Fig. 6.

Experimental data on a resolution phantom shows isotropic resolution and contrast improvement by combining two MPI images acquired using orthogonal channels. (a) Photograph of a resolution acrylic phantom injected with 5× diluted Micromod Nanomag-MIP particles. The laser-cut numbers represent the width and spacing of the channels within each group, with the unit in [mm]. (b-c) Collinear scan acquired with a single y or z channel, showing anisotropic resolution. (d) Combining two orthogonal collinear scans from (b) and (c) achieves isotropic resolution. MPI FOVs for both channels were 2×4.5×5 cm respectively

Author Manuscript Author Manuscript Author Manuscript Author Manuscript

along the x, y, and z directions. The y and z collinear scan times were respectively 3.75 min and 1 min.

Author Manuscript Author Manuscript Author Manuscript Author Manuscript

TABLE I

VARIABLE DEFINITIONS. n IS DIMENSIONALITY OF MPI GRADIENT FIELD.

Notation	Value	Size
x	Spatial Location Vector	$\mathbb{R}^{n\times 1}$
h(x)	Point Spread Function	$\mathbb{R}^{n\times n}$
h_{ij} (x)	i,j^{th} Component of h (x)	$\mathbb{R}^{1}$
E_T (x)	Tangential Envelope	$\mathbb{R}^{1}$
E_N (x)	Normal Envelope	$\mathbb{R}^{1}$
$\mathbf{W}_T$(x), $\mathbf{W}_N$(x)	Tangential and Normal Weighting Matrices	$\mathbb{R}^{n\times n}$
$\mathbf{\Omega}$(x)	Multidimensional Image tensor	$\mathbb{R}^{n\times n}$
$\hat{\rho}_{ij}(\mathbf{x})$	i,j^{th} Component of Ω(x)	$\mathbb{R}^{1}$
$\mathbf{u}_a(t)$, $\mathbf{u}_b(t)$	Excitation and detection vector	$\mathbb{R}^{n\times 1}$
$\hat{\rho}_{\mathbf{u}_a,\mathbf{u}_b}(\mathbf{x},t)$	Image with Tx/Rx Vector $\mathbf{u}_a(t)$ and $\mathbf{u}_b(t)$	$\mathbb{R}^{1}$
$\hat{\rho}(\mathbf{x})$	Isotropic Summed Image	$\mathbb{R}^{1}$
G	Gradient Matrix	$\mathbb{R}^{n\times n}$